ARTICLE

Moisture-Induced Degradation of Quantum-Sized Semiconductor Nanocrystals through Amorphous Intermediates

Hyeonjong Ma, Sungsu Kang, Seunghan Lee, Gisang Park, Yuna Bae, Gyuri Park, Jihoon Kim, Shi Li, Hayeon Baek, Hyeongseung Kim, Jong-Sung Yu, Hoonkyung Lee, Jungwon Park,* and Jiwoong Yang*

Cite This: https://doi.org/10.1021/acsnano.3c03103

Read Online

ACCESS | ⅬⅡ Metrics & More | ▣ Article Recommendations | SI Supporting Information

ABSTRACT: Elucidating the water-induced degradation mechanism of quantum-sized semiconductor nanocrystals is an important prerequisite for their practical application because they are vulnerable to moisture compared to their bulk counterparts. *In-situ* liquid-phase transmission electron microscopy is a desired method for studying nanocrystal degradation, and it has recently gained technical advancement. Herein, the moisture-induced degradation of semiconductor nanocrystals is investigated using graphene double-liquid-layer cells that can control the initiation of reactions. Crystalline and noncrystalline domains of quantum-sized CdS nanorods are clearly distinguished during their decomposition with atomic-scale imaging capability of the developed liquid cells. The results reveal that the decomposition process is mediated by the involvement of the amorphous-phase formation, which is different from conventional nanocrystal etching. The reaction can proceed without the electron beam, suggesting that the amorphous-phase-mediated decomposition is induced by water. Our study discloses unexplored aspects of moisture-induced deformation pathways of semiconductor nanocrystals, involving amorphous intermediates.

KEYWORDS: semiconductor nanocrystals, degradation mechanism, liquid-phase TEM, amorphous intermediates, graphene double-liquid-layer cells
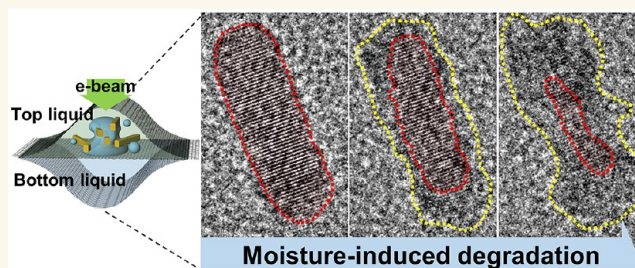
Quantum-confined semiconductor nanocrystals have been widely used in bioimaging systems,[1−3] in optoelectronic devices,[4−6] and as catalysts[7−9] because of their unique properties, such as size- and shape-tunable bandgaps,[10] high photoluminescence quantum yields, and sharp emission spectra.[11] They are intrinsically less stable than their bulk counterparts,[12,13] because of their high surface-to-volume ratio, and are especially vulnerable to decomposition by the presence of water and oxygen that are inherent in their practical applications. There have been several reported attempts to increase the stability of semiconductor nanocrystals by controlling their structures with an aim to modulate their interactions with water molecules.[14] A mechanistic understanding of the degradation of semiconductor nanocrystals, with focusing on structure transformation pathways during nanocrystal deformation, can facilitate the design and synthesis of highly stable nanocrystals with robust structures. In addition, it is important to investigate structural deformation of nanocrystals in atomic-scale spatial resolution because minor variations in their atomic arrangements can significantly change their properties.[15−18]

However, previous studies have typically focused on studying changes in the photophysical properties of semiconductor nanocrystals during the degradation process without tracing the real-time structural changes.[19,20]

Changes in nanostructures during chemical processes have been observed by optical or X-ray techniques, such as absorption spectroscopy, X-ray scattering, and X-ray diffraction analysis methods.[21−25] For example, *in-situ* absorption spectroscopy has been extensively used for studying semiconductor nanocrystal formation and degradation processes.[26,27] These spectroscopic techniques can provide information about the average structural changes of nanocrystals from a large population in ensembles. When the reaction pathways are

A
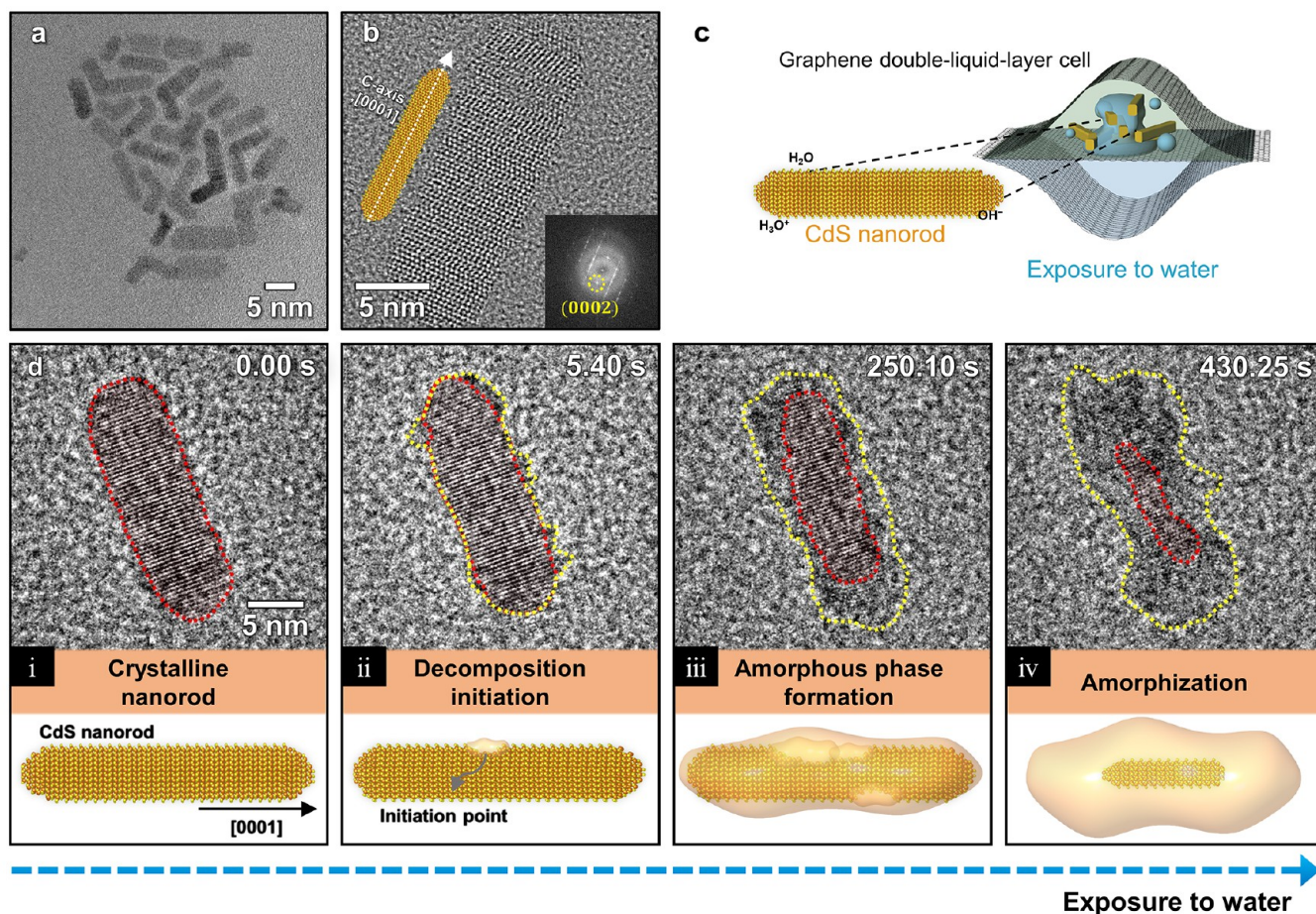
Figure 1. Moisture-induced degradation of CdS quantum nanorods. (a, b) TEM images of CdS nanorods used in this study. **(c)** Schematic illustration of the *in-situ* liquid-phase TEM experiments for studying moisture-induced degradation of semiconductor nanocrystals. **(d)** TEM images of the representative reaction stages of amorphous-phase-mediated decomposition of CdS nanorods. The areas highlighted with red and yellow dashed lines represent crystalline and amorphous phases, respectively. The corresponding schematic illustrations are also shown. Please note that there are inherent limitations in fully describing the three-dimensional structure from TEM images, as they only provide two-dimensional projections. The corresponding video is shown in Video S1.

inferred based on averaged signals, critical events existing in the individual chemical pathways can be missing. Recent studies of nanomaterial transformations report the involvement of various intermediate states, highlighting the importance of tracking structure changes of individual nanocrystals.[28−34] For example, it was revealed that the nanocrystal formation process includes the coexistence of various intermediate states such as an amorphous phase, providing an important free-energy landscape for crystallization.[32,33] However, for the deformation of quantum-sized semiconductor nanocrystals, a mechanistic understanding is weak and requires tracking decomposition trajectories of individual nanocrystals to answer questions regarding the existence and roles of intermediate states.

In-situ liquid-phase transmission electron microscopy (TEM) can directly visualize structural changes in individual nanocrystals with high spatial (sub-nanometer) resolution.[35−40] The control over the reactions of nanocrystals during liquid-phase TEM is usually limited to electron-beam-induced reactions.[41−44] Reactions of noble metal nanocrystals induced by radiolysis products are representative examples of these works.[38,42] Microfabricated cells can be modified to flow-type cells, such that the initiation of the reaction can be controlled by regulating the introduction of chemicals through inlets (Figure S1).[45,46] However, effective imaging is

challenging because of strong electron beam scattering by thick liquid layers (typically >100 nm)[47,48] and unwanted sample movement caused by the liquid flow. Graphene liquid cells achieve the atomic spatial resolution owing to the reduced electron beam scattering.[49−51] Nonetheless, conventional graphene liquid cells require all reactants to be mixed before their loading, preventing control of the initiation of the reaction (Figure S1). Although liquid cells using MoS_2 separator membranes have been reported to overcome this limitation,[52,53] Mo and S atoms with relatively higher atomic numbers can hinder the clear observations of objects of interest in a liquid by providing significant background contrast. The transfer process of MoS_2 usually requires protective polymer layers, which can remain as contaminations in TEM imaging.[54] Thus, advanced liquid cells capable of high-resolution imaging and reaction control by *in-situ* mixing of the chemicals are in high demand, especially to facilitate the study of the deformation mechanisms of quantum-sized nanocrystals and the possible intermediate states formed during this process.

Herein, we studied moisture-induced degradation pathways of quantum-sized CdS semiconductor nanorods using graphene double-liquid-layer-cell (GDLC) electron microscopy. GDLCs use ultrathin graphene separators to regulate the mixing of encapsulated liquids and are thus capable of imaging
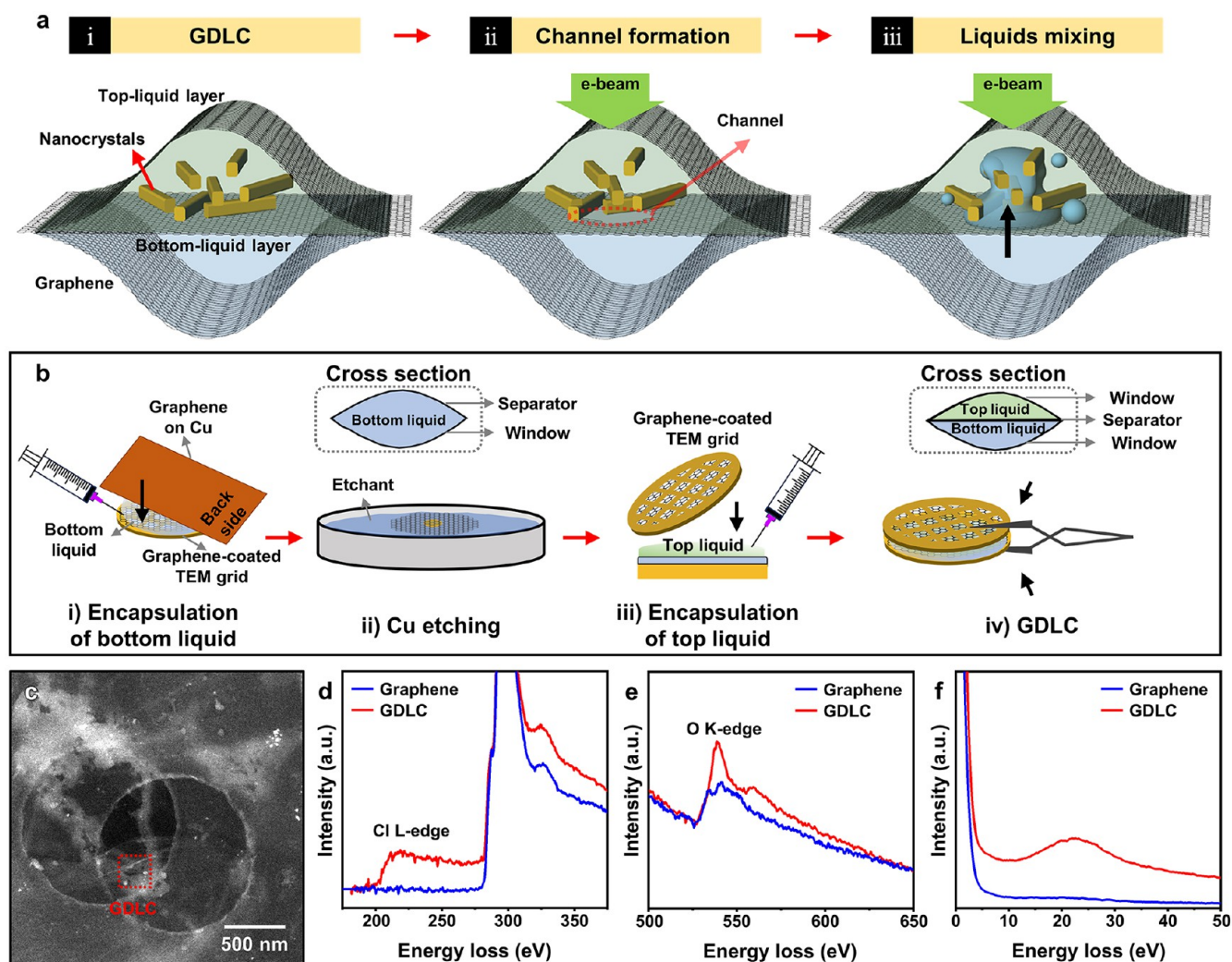
Figure 2. Development of advanced liquid cells capable of reaction control. (a) Schematic illustration of the working mechanism of GDLCs. (i) Two liquid layers are separated by a separator. (ii) Channels connecting the liquid layers are formed upon electron-beam-radiation-induced damage of the separator. (iii) Reactions are initiated by liquid mixing via the formation of channels. (b) Schematic of the process for fabricating GDLCs; a detailed illustration is provided in Figure S7. (c) HAADF-STEM image of a GDLC encapsulating water and 1,2-dichlorobenzene. (d,e) High-loss and (f) low-loss EELS spectra acquired from the red boxed area in Figure 2c. For comparison, the spectra of the dried graphene (acquired from the blue boxed area in Figure S8a) are shown together.

the entire chemical reaction process at near-atomic resolution. Therefore, it was possible to track the structural changes of CdS quantum nanorods upon the introduction of water. During the nanorod degradation, we observed that noncrystalline amorphous domains, composed of $Cd(OH)_x$, were formed at the CdS nanorod surfaces and grew into the nanorod interior. The shape evolution of CdS nanorods, accompanied by the formation of the amorphous domains, was distinguishable from the behavior observed in conventional nanocrystal etching where the amorphous intermediates are not involved.[55−57] The observed process occurred even without the electron beam, suggesting that water itself can induce amorphous-phase-mediated decomposition. These results imply that the degradation of semiconductor nanocrystals can involve diverse pathways, including nonclassical decomposition processes.

RESULTS AND DISCUSSION

Moisture-Induced Degradation of CdS Quantum Nanorods. CdS quantum nanorods were prepared (see

Methods) to investigate the degradation mechanism of quantum-sized semiconductor nanocrystals by water.[58] Cd-chalcogenides are regarded as the most representative material for studying quantum-sized semiconductor nanocrystals, because their superior optical/electrical properties can be precisely manipulated by the well-developed synthesis methods.[5,10,11,58] TEM and X-ray diffraction analyses confirm that wurtzite-CdS nanorods were well synthesized with an average diameter of ∼5 nm and a length of ∼15 nm (Figure 1a,b, and Figures S2−S5). TEM images show that wurtzite-CdS nanorods have anisotropic shapes elongated along the *c*-axis. The direct relationship between the crystal orientation and the shape of nanocrystals makes observation of the crystal-orientation-dependent decomposition process straightforward.

We used *in-situ* liquid-phase TEM to reveal the moisture-induced degradation mechanism of quantum-sized semiconductor nanocrystals (Figure 1c). Because of the limitations stated in the introduction, previous works have focused on the etching processes controlled by the radiolysis products of the electron beam.[38,42,44,55−57] To overcome this limitation, we

developed advanced liquid cells (graphene double-liquid-layer cells) that allow control of the initiation of chemical reactions during atomic-resolution liquid-phase TEM; their fabrication process and working mechanism are discussed in the next section. Figure 1d and Video S1 reveal the representative reaction stages of the moisture-induced degradation process of CdS quantum nanorods. Initially, a highly crystalline nanocrystal was observed. Notably, an amorphous phase, highlighted by the yellow dashed lines shown in Figure 1d, was observed during the decomposition process; this region had high contrast with respect to the background solution but did not show crystalline lattices, implying the formation of an amorphous phase. The decomposition process of the CdS nanorods is described by four steps: (i) crystalline nanorods, (ii) decomposition initiation, (iii) amorphous phase formation, and (iv) amorphization of the entire outer region.

Development of Graphene Double-Liquid-Layer Cells. The structure of GDLCs is similar to that of conventional graphene liquid cells except that an additional thinner graphene sheet (e.g., single- or trilayers) is used as the separator. Thicker multilayer graphene (e.g., ~6−8 layers) is used as windows to guarantee the liquid encapsulation (see Methods). Thus, we can expect that the proposed GDLCs maintain the advantages of graphene liquid cells (high imaging resolution, repeatable observation over a large number of liquid pockets, and reduced effects of heating/charging[49,51]), while providing the additional ability to control chemical reactions. The following describes the proposed working mechanism of the GDLCs. (i) Two different liquid solutions are encapsulated as the top and bottom liquid layers, which are separated by an ultrathin graphene separator to prevent the mixing of liquids. (ii) A channel is formed in the separator using the electron beam to connect the two chambers, which allows the liquid to mix. (iii) The reaction is initiated when the two liquids mix via the channels (Figure 2a). Therefore, the two liquids are prevented from reacting before electron beam irradiation of the regions of interest. Using the acceleration voltage of TEM (200−300 kV) higher than the knock-on threshold voltage of graphene (~86 kV[59]) where graphene can be further chemically reacted with radiolysis products generated by electron beam irradiation,[60] we expect that the thinnest graphene (i.e., the separator) would be degraded, while thicker windows keep encapsulating the liquid. We used the electron flux density of 500−1500 e⁻/Å²·s in this study, which is similar to (or lower than) those used in previous works on graphene liquid cells based on multilayer graphene to avoid window damage (Table S1). To further verify the perforation of the graphene separator during liquid-phase TEM imaging, we studied the electron beam-induced damage of graphene membrane using a modified double-liquid layer cells which used amorphous carbon films (10 nm) and trilayer graphene as top/bottom windows and a separator, respectively (see Methods and Figure S6). The results clearly show that a graphene separator is broken after electron beam irradiation.

The fabrication process of GDLCs is illustrated in Figure 2b, Methods, and Figure S7. Briefly, graphene windows were prepared by direct transfer of multilayer graphene onto holey carbon TEM grids.[61] The first liquid sample (called the bottom liquid) was encapsulated between the graphene-coated grid and the thinner graphene separator on Cu foil (i, Figure 2b). The Cu foil was removed by etching (ii, Figure 2b) and the structure of the liquid cell, at this moment, is similar to that of a conventional graphene liquid cell,[48−51] except that the

graphene-coated TEM grid was present on only one side (Figure S7). The second liquid sample (called the top liquid) was encapsulated between the graphene separator (iii, Figure 2b) and the additional graphene-coated grid (iv, Figure 2b). To verify that the suggested double-liquid-layer cell was constructed properly, we carried out electron energy-loss spectroscopy (EELS) analysis on GDLCs encapsulating 1,2-dichlorobenzene and water. The EELS spectra of water in the graphene liquid cells show oxygen core-loss peaks of water at 535 and 556.4 eV,[62] and the plasmon peak of water at 22.7 eV (Figure S8).[63,64] The spectrum of 1,2-dichlorobenzene exhibits the L-edge signal of chlorine at ~200 eV (Figure S9).[65] EELS spectra of 1,2-dichlorobenzene/water double-liquid layers encapsulated in GDLCs simultaneously show all of these signals (Figure 2c−f and Figure S10 for the entire spectrum), confirming that water and 1,2-dichlorobenzene were superimposed. Furthermore, the probability for the formation of the liquid pocket in each hole (i.e., holes of Quantifoil films) of overlapped TEM grids forming GDLCs was investigated by using atomic-force microscopy (AFM) (Supporting Method). The presence of liquid pockets was determined by height profiles (Figure S11), and ~90% of holes for each side (i.e., top and bottom) contained liquid pockets. This suggests that overlapping of top and bottom liquid pockets is highly probable in GDLCs when the top and bottom grids are aligned well.

Indeed, the fact that we can observe the decomposition of CdS nanocrystals is strong evidence of the successful operation of the suggested GDLCs. In a control experiment, the shape of CdS nanocrystals dispersed in toluene (without water exposure) was preserved (Figure S12 and Video S2), implying that the decomposition of CdS nanocrystals was initiated after mixing of the top and bottom solutions. In addition, the time required for channel formation in GDLCs increases with increasing thickness of the graphene separators (Figures S13 and S14), suggesting that thicker graphene is more tolerable against electron beam irradiation. This is consistent with the fact that the encapsulation of the liquid was maintained during the reaction period (>10 min) after the channel formation because of the use of multilayer graphene windows. The results verify that the proposed GDLCs are a reliable tool for *in situ* liquid-phase TEM studies of chemical reactions. It is expected that *in situ* liquid-phase TEM imaging would be possible for various chemical reactions by tailoring the combination of the liquid layers (see Supporting Methods, Figure S15, and Video S3 for etching of gold nanorods in GDLCs).

Amorphization of CdS Quantum Nanorods. We analyzed the decomposition process of the CdS quantum nanorods in detail. The use of the GDLCs provides several advantages compared to previously reported graphene liquid cells.[48−51] It enables on-demand initiation of the reaction and atomic-resolution imaging required for tracking the decomposition of CdS nanorods and the reaction intermediates, which have a relatively low TEM contrast. TEM images using GDLCs even showed superior contrast compared to that obtained with dried samples on a single-layer MoS₂ membrane (Figures S16−S18), demonstrating the advantages of GDLCs for liquid-phase TEM imaging of low-Z-contrast materials such as amorphous species. We observed that the amorphous-mediated decomposition reproducibly occurred for a large number of nanocrystals regardless of the initial organic solvent (toluene or 1,2-dicholobenzene) for nanocrystals. Time-series TEM images of four representative nanocrystals (denoted as
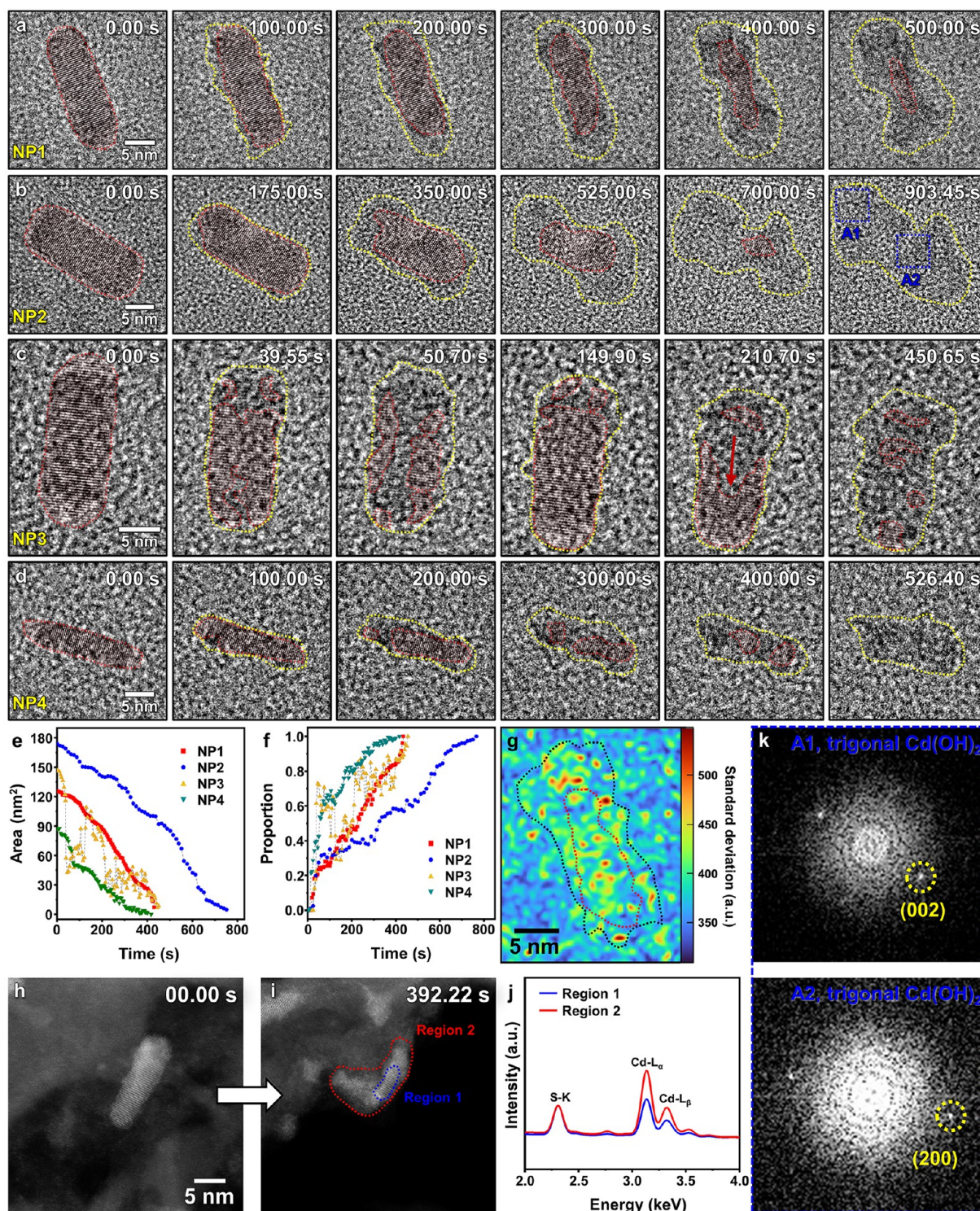
Figure 3. Amorphization of CdS quantum nanorods. (a−d) Time-series TEM images of water-induced degradation of CdS nanorods denoted as NP1−NP4. The initial solvent for the nanocrystals was toluene except for NP4 (1,2-dichlorobenzene). The corresponding videos are shown in Videos S1 and S4−S6. (e) Time-dependent changes in the crystalline area for NP1−NP4. (f) Time-dependent changes in proportion of amorphous-phase area to overall area for NP−NP4 from the first snapshots in (a)−(d). (g) Color map of the standard deviation (350−370 s from (a)) of contrast for each pixel. Black and red dotted lines represent boundaries of amorphous and crystalline phases at 350 s, respectively. (h, i) HAADF-STEM images showing the amorphous-phase-mediated decomposition. (j) EDS spectra corresponding to regions 1 and 2 in (i). (k) FFT patterns corresponding to regions A1 and A2 in the sixth snapshot of (b).

NP1−NP4) are displayed in Figure 3a−d (Videos S1 and S4−S6). The suppressed thermal motion of nanocrystals is attributed to the increased shear viscosity[66,67] and the interaction between graphene and surface ligands.[68]
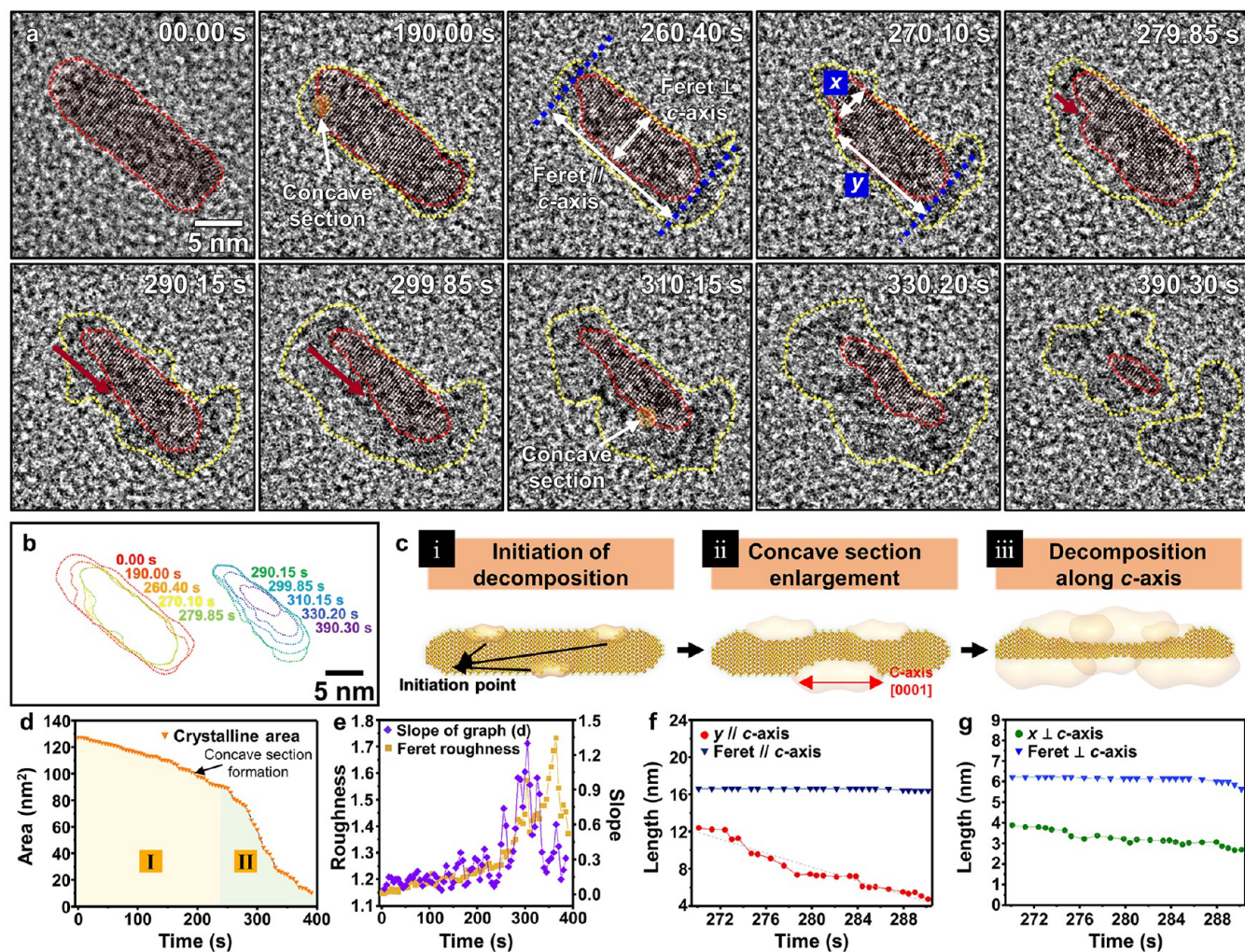
Figure 4. Shape-evolution of crystalline phases during nanorod degradation. (a) Time-series of TEM images showing anisotropic etching of crystalline phases. Areas highlighted with red and yellow dashed lines represent crystalline and amorphous phases, respectively. The corresponding video is shown in Video S7. (b) Contour plots of the crystalline area. (c) Schematic illustration of unconventional anisotropic etching during amorphous-phase-mediated decomposition. (d) Time-dependent change in projected crystalline area. (e) Changes of Feret roughness and gradient of the curves in (d). (f) Time-dependent change in y and Feret diameter parallel to the c-axis. (g) Time-dependent change in x and Feret diameter vertical to the c-axis.

The projected crystalline area decreased over time (Figure 3e), suggesting that the nanocrystals continuously decomposed during the reaction process. Interestingly, the overall particle area (sum of crystalline and amorphous areas) did not necessarily decrease and fluctuated with irregular deviation (Figure S19), which reflects the continuous formation and dynamic behaviors of the amorphous species. In addition, the ratio of the amorphous area to the overall particle area increased over time (Figure 3f), implying that the crystalline phase was transformed into the amorphous phase during decomposition. For several cases including NP3, we could observe the decomposition process from the different viewing directions, showing the overlap of the crystalline domain with the amorphous phase along the viewing direction from the initiation of the decomposition (Figures S20 and S21 and Video S5). This confirms that the nanorod decomposition initiated at random locations of the nanocrystal surface. Furthermore, concealment and reappearance of the lattice fringes suggests the dynamic motion of amorphous species in the liquid medium. Furthermore, color maps of the standard

deviation of contrast (for 350−370 s from Figure 3a) show that the amorphous phase had higher standard deviation values than those of the background and crystalline phase (Figure 3g and Supporting Methods), which is attributed to the dynamic atomic motion.[69] In previous studies, the existence of amorphous intermediates during the growth of nanocrystals was revealed by TEM and AFM analyses.[70−72] Our observations suggest that the amorphous species can exist as an intermediate state during the degradation of nanocrystals.

Notably, the chemical composition of the amorphous species was verified by liquid-phase TEM analysis. High-angle annular dark-field scanning transmission electron microscopy (HAADF-STEM) images clearly show the formation of amorphous phases (Figure 3h,i). The results of energy-dispersive X-ray spectroscopy (EDS) analysis suggest that the amorphous species are Cd-rich compounds, while the crystalline part maintains a stoichiometric ratio (1:1) of Cd and S (Figure 3j). When we carried out *in-situ* liquid-phase TEM imaging on the decomposition process for a prolonged reaction time (∼15 min), the amorphous species was partially
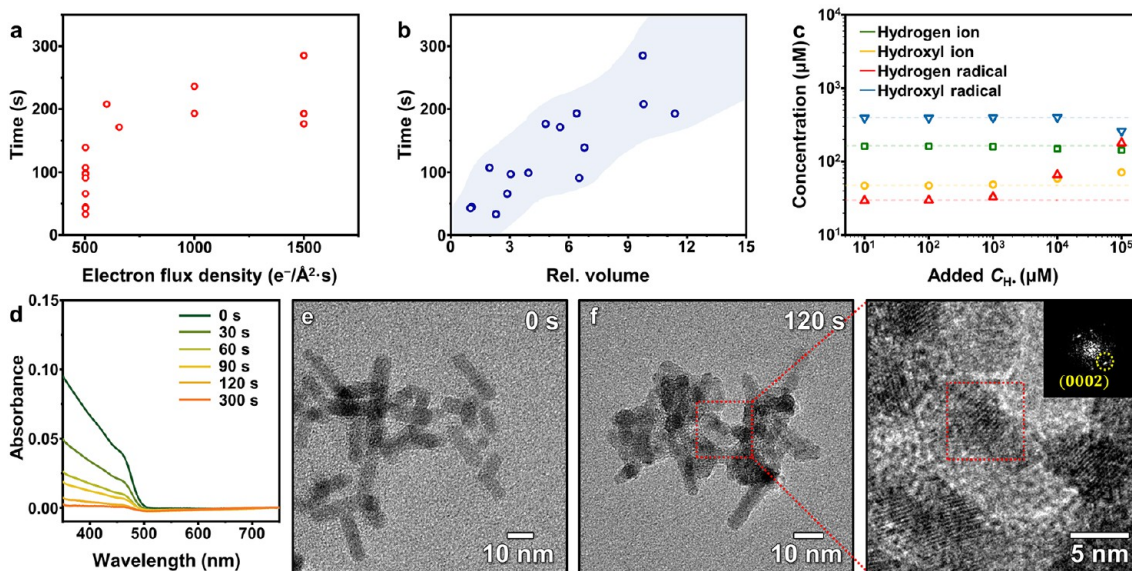
Figure 5. Investigation of the electron beam effect. Time required to obtain 50% of the initial projected crystalline area ($t_{1/2}$) as a function of (a) the electron flux density and (b) initial volume of the nanocrystal. (c) Calculated steady-state concentration of hydrogen and hydroxyl radicals/ions in water as a function of the additional concentration of hydrogen radicals (electron flux density: 1000 e$^-$/Å^2·s). The dashed lines indicate the steady-state concentrations of each species for pure water radiolysis. (d) Time-dependent changes of absorption spectra of the solution containing CdS nanorods after water exposure. TEM images of CdS nanorods (e) before and (f) after the water exposure.

crystallized (see the last snapshot of Figure 3b). The fast Fourier transform (FFT) patterns acquired from regions A1 and A2 show spots corresponding to (002) and (200) planes of Cd(OH)$_2$, respectively (Figure 3k), suggesting that the composition of the amorphous species is based on Cd(OH)$_x$. Additional TEM images showing partially crystallized Cd-(OH)$_2$ with amorphous species are provided in Figure S22. The following decomposition mechanism of CdS quantum nanorods is proposed. First, CdS nanocrystals are partially dissolved (from the surface) into cadmium ions by reacting with hydrogen ions in the water (CdS + 2H$^+$ → Cd^{2+} + H$_2$S).[73] The concentration of hydroxyl ions rapidly increases, considering the small volume of water miscible in organic solutions.[74] Therefore, the generation of cadmium hydroxide is facilitated by the reaction Cd^{2+} + 2OH$^-$ ⇌ Cd(OH)$_2$, during which amorphous Cd(OH)$_x$ is formed on the surface of the CdS nanorods. This can explain the observed dynamic motion of the amorphous species, considering that Cd(OH)$_2$ is partially soluble in water.

Shape Evolution of Crystalline Phases during Nanorod Degradation. The shape evolution of the crystalline domains was studied during the amorphous-phase-mediated decomposition process, showing the unconventional anisotropic etching of the nanocrystals (Figure 4a,b and Video S7). Please note that "etching" describes the changes in the crystalline parts, while "decomposition" is related to the entire particles. The CdS nanorods show unique morphological changes during decomposition, which have not been previously observed during conventional etching of metal nanocrystals. Once the etching was initiated at a random location where the crystal surface was directly exposed to water molecules by partial ligand detachment, the CdS nanorods had both partially etched and nonetched parts, even on the same plane. This resulted in the formation of concave sections (Figure 4a) that increased the roughness of the nanocrystal surface. Conventionally, etching starts from high-energy surfaces and the etched crystals show smooth crystal surfaces during a

continuous decrease in crystal volume; the morphological changes of the crystals during etching have been explained by the thermodynamics related to the surface energy of each facet. For example, the etching of metal nanocrystals results in facet-selective anisotropic changes in the morphology, and each facet has a very smooth surface.[55−57]

The rate of etching increased after the initiation of the reaction, as shown by the crystals with rough surfaces, which gradually formed concave sections that subsequently grew (Figure 4c). Time-dependent changes in the crystalline area showed two distinct stages: (I) slowly decreasing and (II) abruptly decreasing stages after the formation of the concave sections (Figure 4d). We studied the correlation between the roughness of the crystal boundary and the time-dependent areal decomposition rate (Figure 4e) that is defined as the slope of Figure 4d. The areal decomposition rate increased markedly at ∼235.15 s as the Feret roughness increased (Figure S23 for the definition). This suggests that crystals with rough boundaries decompose faster than crystals with smooth boundaries. The rapid etching near the concave sections is presumably due to the loss of ligand passivation on the surface where etching is initiated. Because the amorphous phase impedes the direct exposure of the nanocrystal surface to water, the irregular crystal shape evolution becomes highly probable during the amorphous-phase-mediated decomposition process.

For further quantitative analysis of the decomposition rate in the concave section, two additional parameters are introduced (x and y in the fourth snapshot of Figure 4a; see Figure S24 for their definition). The length y indicates the shortest distance between the tangent of the nanorod vertical to the c-axis (blue dotted line) and the point where the crystalline boundary begins to bend into the concave section of the crystal. The length x indicates the diameter at a selected point in the concave section of the nanorods after partial decomposition. In Figure 4f and 4g, x and y are compared with the Feret diameters perpendicular and parallel to the c-axis, respectively.

The rate of decrease in the Feret diameters represents the decomposition rate of the entire crystal along the corresponding direction. The rate of decrease in y was considerably higher than that in the Feret diameter parallel to the c-axis. The results indicate a higher decomposition rate along the c-axis in the ligand-detached concave section than that in the ligand-passivated original surfaces. Furthermore, quantitative analysis of the correlation between the rate of decrease in y and local curvatures in the concave section suggests that high local curvatures facilitate rapid etching of the nanorod ([Figures S25 and S26]). The lower decomposition rate of the ligand-passivated surface may be attributed to the surface-stabilizing effect by passivating the dangling bonds of the surface atoms.[75] The rate of decrease in y was much higher than that in x, suggesting that the decomposition rates of crystals without surface-ligand passivation are determined by the intrinsic surface energy of the crystal facets, bearing in mind that wurtzite crystals show the highest surface energy on the (0001) surface ([Figure S27]).[75]

Investigation of the Electron Beam Effect. Because electron beam radiation is inevitable during TEM measurements, it is important to understand its effect on the observed process. The decomposition rate of the CdS nanorods in accordance with the electron flux density is summarized in [Figure 5a]; however, a clear dependency is not observed. The decomposition rate decreased with increasing volume of nanorods ([Figure 5b]), suggesting that the interface between the nanorod and etching solutions is more important than the electron flux density for determining the decomposition rate. Moreover, we conducted electron beam blocking experiments during in situ TEM imaging ([Figure S28]). The electron beam was blocked after the initiation of decomposition (i.e., after channel formation between the two liquid layers). The result shows that the amorphous-phase-mediated decomposition proceeded without an electron beam. This suggests that the reactive radicals formed by radiolysis are not necessary for the observed degradation mechanism, although we cannot exclude the possibility that the radiolysis products accelerate the process.

To better understand the effect of electron beam irradiation on the composition of the water, we carried out radiolysis simulations[76] considering additional hydrogen radicals, one of the representative products of toluene radiolysis,[67] on the water radiolysis. In this simulation, hydrogen radicals with various concentrations were additionally introduced to the water at steady-state under the electron beam ([Figure 5c] and [Figure S29]). Interestingly, the calculated steady-state concentrations of H^+ and OH^- do not change significantly, while those of hydroxyl radicals (one of the representative etchants for nanocrystals in liquid-phase TEM experiments[38,42,77]) decrease when increasing the amount of additional hydrogen radicals. Considering the additional radical scavenging effect of organic molecules,[78] the results imply that the effect of the electron beam is even suppressed for our system, compared to previous works studied in the aqueous system for liquid-phase TEM imaging.

We further investigated the effect of the water exposure on semiconductor nanocrystals with ex-situ experiments outside of the TEM column. The toluene solution containing CdS nanorods was mixed with water, and a series of aliquots drawn from the mixture was analyzed by optical spectroscopy and TEM (see [Supporting Methods]). The intensities of the band-edge transitions in the absorption spectra diminished over time

([Figure 5d] and [Figure S30]), suggesting the degradation of CdS nanorods by exposure to water. In a control experiment, CdS nanorods dispersed in toluene without exposure to water gave absorption spectra with constant shapes and intensities ([Figure S31]). In addition, the TEM images of CdS nanorods after water exposure display aggregated nanostructures without lattice fringes ([Figure 5e] and [5f]), characteristic of the amorphous materials. Furthermore, the examination of reaction intermediates during the water-induced degradation of dried CdS nanocrystals, through either direct water exposure or exposure to humid air, yielded similar results ([Figures S32 and S33]). These ex-situ experimental results are consistent with those acquired from in-situ liquid-phase TEM observations. It can be concluded that reactions under a normal environment can be reproduced in the TEM column for direct imaging with a considerable degree of similarity.

CONCLUSIONS

In this study, we investigated the amorphous-phase-mediated decomposition of semiconductor nanocrystals using GDLCs, which enable real-time atomic-scale observation of the entire reaction process from initiation to termination. The advanced in-situ liquid-phase TEM imaging allowed microscopic characterization of the dynamic changes occurring within individual nanocrystals, which is challenging to achieve through ex-situ analysis. We could unveil crucial insights into various aspects of moisture-induced degradation of semiconductor nanocrystals, including the formation and chemical composition of amorphous intermediates, detailed degradation trajectories such as irregular shape evolution, and the influence of the local features. The presence of high-contrast domains without lattice fringes in the TEM images implied the formation of amorphous phases, which was also supported by the results of standard deviation mapping, dynamic atomic motion of the amorphous domains, and ex-situ experiments. The chemical composition of the amorphous species can be assigned as $Cd(OH)_x$, which was confirmed by EDS and in situ TEM analyses. The irregular shape evolution of CdS crystals during the amorphous-phase-mediated decomposition was quite different from that of conventional etching processes.[55−57] Our findings provide insights into the deformation mechanism of quantum-sized semiconductor nanocrystals at the atomic level. For example, our result can explain why moisture exposure dramatically and irreversibly degrades the optical properties of quantum-sized semiconductor nanocrystals. The amorphous layers would act as trap sites to induce nonradiative recombination of excitons, and their formation seems to be irreversible considering their chemical composition. We envision that our results will be helpful for developing strategies for designing highly stable semiconductor nanocrystal quantum dots.

METHODS

Synthesis of CdS Quantum Nanorods. Colloidal CdS quantum nanorods were prepared by following a modified version of a previously reported method.[58] CdS nanorods were synthesized by the reaction between metal−oleylamine complexes and sulfur−oleylamine solutions. In a typical synthesis, metal-oleylamine complexes were prepared by dissolving $CdCl_2$ (0.75 mmol) in 10.0 mL of oleylamine at 120 °C for 2 h. A sulfur−oleylamine solution was prepared by dissolving elemental sulfur (2.25 mmol) into 2.5 mL of oleylamine. The sulfur−oleylamine solution was injected into the solution of the metal−oleylamine complex at 100 °C and then kept at this temperature for 3 h. The products (i.e., CdS quantum nanorods)

were purified by the standard centrifugation method using ethanol. A few drops of trioctylphosphine were used to remove excessive sulfur precursors. The synthesized nanorods can be dispersed in various nonpolar solvents, and CdS nanocrystals in toluene (0.15 mM, based on Cd) were used for further experiments unless otherwise stated.

Preparation of Graphene Double-Liquid-Layer Cells. GDLCs were prepared as follows. The detailed schematic illustration showing the fabrication procedure of GDLCs is shown in Figure S7. In a typical process, graphene-coated holey carbon TEM grids were prepared by the direct transfer[61] of multilayer graphene that was used as windows for the GDLCs. A drop (less than 1 μL) of the bottom liquid (deionized water in this study) was deposited on the graphene of the as-prepared graphene-coated TEM grid (i, Figure S7). The thinner separator membrane (single- or trilayer graphene on Cu foil) was placed onto the bottom liquid layer on the graphene-coated TEM grid. Excess solution was removed by mild vacuum suction, where the strong interaction between the two graphene sheets encapsulated the liquid (ii) (Figure S7). Then, the Cu foil was etched by placing a graphene grid/bottom liquid/graphene separator/Cu in ammonium persulfate solution (0.2 M) (iii, Figure S7). After etching of the Cu foil, the grid (graphene grid/bottom liquid/graphene separator) was gently lifted using tweezers (Figure S7). Then, a tiny drop (less than 1 μL) of the top liquid (nanocrystal solution in this study) was deposited on the graphene separator of the grid (v, Figure S7). Finally, another multilayer graphene-coated grid was carefully positioned on the top liquid layer (vi, Figure S7), such that the graphene side of the graphene-coated grid can be attached to the graphene separator. The as-prepared GDLCs were squeezed with tweezers to promote the attachment of two grids and the encapsulation of the liquids (vii, Figure S7, graphene grid/bottom liquid/graphene separator/top liquid/graphene grid). As was done for the bottom liquid, excess solution was removed using gentle vacuum suction. The GDLCs can be modified by changing top/bottom windows with the other type of thin membrane while maintaining the liquid separator as the graphene membrane. Amorphous carbon films were used as windows for verification of graphene separator perforation (Figure S6).

***In-Situ* Transmission Electron Microscopy.** TEM images were recorded on a Titan Themis Z (FEI, Thermo Fisher Scientific) at an operation voltage of 300 kV and a Tecnai G2 F20 TWIN TMP (FEI, Thermo Fisher Scientific) at an operation voltage of 200 kV. Titan Themis Z was operated with a high-brightness electron gun (x-FEG), image corrector (CETCOR, hexapole-type Cs-corrector), probe corrector (DCOR, hexapole-type Cs-corrector), and a Ceta2 camera (4k × 4k pixels, 16-bit dynamic range, and 40 frames per second). The spatial resolution was ~60 pm in TEM/STEM modes. *In-situ* data for the decomposition of CdS nanorods were acquired with a Titan Themis Z. Tecnai G2 F20 TWIN TMP was operated with a ZrO/W (100) Schottky emitter electron gun with high maximum beam current (>100 nA). The point and line resolution were 0.27 and 0.155 nm, respectively. For liquid-phase TEM analysis, we used the area where holes (coated by graphene) of the top and bottom holey carbon films were overlapped (Figure 2c). With our Titan Themis Z, the electron flux density can be adjusted accurately (in the continuous number) using a monochromator that can control the gun lens. The data were processed with FIJI software, and codes were developed in house. All TEM data were exported in MP4 format for publication, and image analyses of the decomposition process were conducted with original images.

ASSOCIATED CONTENT

Ⓢ Supporting Information

The Supporting Information is available free of charge at https://pubs.acs.org/doi/10.1021/acsnano.3c03103.

> Supporting methods; characterization of CdS quantum nanorods; FFT analysis of the graphene separator; schematic of the fabrication procedure of GDLCs; EELS analysis of conventional graphene liquid cells and GDLCs; liquid-phase TEM images of CdS nanorods in a graphene liquid cell without water; effects of the separator thickness; TEM imaging of samples in GDLCs and on single-layer MoS_2 under vacuum; time-dependent changes in the overall area and proportion of amorphous-phase area to overall area; TEM images showing amorphous-phase-mediated decomposition in different directions; TEM images showing partially crystallized amorphous species; definition of Feret parameters and x and y; surface energy of wurtzite CdS crystals; electron beam blocking experiment; radiolysis simulation for water; *ex-situ* degradation of CdS quantum nanorods (PDF)

> Video S1: Video showing the amorphous-phase-mediated decomposition process (MP4)

> Video S2: Video showing the CdS nanorod under the electron beam irradiation in a graphene liquid cell without water exposure (MP4)

> Video S3: Video showing the gold nanorod etching in a GDLC (MP4)

> Video S4: Video showing crystallization of the amorphous phase after decomposition of a CdS nanorod (MP4)

> Video S5: Video showing overlap of the crystalline domain with the amorphous domain (MP4)

> Video S6: Video showing the amorphous-phase-mediated decomposition process in 1,2-dichlorobenzene and water (MP4)

> Video S7: Video showing unconventional anisotropic etching of the crystalline domain (MP4)

AUTHOR INFORMATION

Corresponding Authors

Jungwon Park − *Center for Nanoparticle Research, Institute for Basic Science (IBS), Seoul 08826, Republic of Korea; School of Chemical and Biological Engineering, and Institute of Chemical Processes and Institute of Engineering Research, College of Engineering, Seoul National University, Seoul 08826, Republic of Korea; Advanced Institute of Convergence Technology, Seoul National University, Suwon-si, Gyeonggi-do 16229, Republic of Korea;* ⓸ orcid.org/0000-0003-2927-4331; Email: jungwonpark@snu.ac.kr

Jiwoong Yang − *Department of Energy Science and Engineering, Daegu Gyeongbuk Institute of Science and Technology (DGIST), Daegu 42988, Republic of Korea; Energy Science and Engineering Research Center, Daegu Gyeongbuk Institute of Science and Technology (DGIST), Daegu 42988, Republic of Korea;* ⓸ orcid.org/0000-0002-2346-8197; Email: jiwoongyang@dgist.ac.kr

Authors

Hyeonjong Ma − *Department of Energy Science and Engineering, Daegu Gyeongbuk Institute of Science and Technology (DGIST), Daegu 42988, Republic of Korea*

Sungsu Kang − *Center for Nanoparticle Research, Institute for Basic Science (IBS), Seoul 08826, Republic of Korea; School of Chemical and Biological Engineering, and Institute of Chemical Processes, Seoul National University, Seoul 08826, Republic of Korea*

Seunghan Lee − *Department of Physics, Konkuk University, Seoul 05029, Korea*

Gisang Park − *Department of Energy Science and Engineering, Daegu Gyeongbuk Institute of Science and Technology (DGIST), Daegu 42988, Republic of Korea*

Yuna Bae − *Center for Nanoparticle Research, Institute for Basic Science (IBS), Seoul 08826, Republic of Korea; School of Chemical and Biological Engineering, and Institute of Chemical Processes, Seoul National University, Seoul 08826, Republic of Korea*

Gyuri Park − *Department of Energy Science and Engineering, Daegu Gyeongbuk Institute of Science and Technology (DGIST), Daegu 42988, Republic of Korea*

Jihoon Kim − *Center for Nanoparticle Research, Institute for Basic Science (IBS), Seoul 08826, Republic of Korea; School of Chemical and Biological Engineering, and Institute of Chemical Processes, Seoul National University, Seoul 08826, Republic of Korea;* orcid.org/0000-0003-2760-2610

Shi Li − *Department of Energy Science and Engineering, Daegu Gyeongbuk Institute of Science and Technology (DGIST), Daegu 42988, Republic of Korea*

Hayeon Baek − *Center for Nanoparticle Research, Institute for Basic Science (IBS), Seoul 08826, Republic of Korea; School of Chemical and Biological Engineering, and Institute of Chemical Processes, Seoul National University, Seoul 08826, Republic of Korea*

Hyeongseung Kim − *Department of Energy Science and Engineering, Daegu Gyeongbuk Institute of Science and Technology (DGIST), Daegu 42988, Republic of Korea*

Jong-Sung Yu − *Department of Energy Science and Engineering, Daegu Gyeongbuk Institute of Science and Technology (DGIST), Daegu 42988, Republic of Korea; Energy Science and Engineering Research Center, Daegu Gyeongbuk Institute of Science and Technology (DGIST), Daegu 42988, Republic of Korea;* orcid.org/0000-0002-8805-012X

Hoonkyung Lee − *Department of Physics, Konkuk University, Seoul 05029, Korea;* orcid.org/0000-0002-6417-1648

Complete contact information is available at:
https://pubs.acs.org/10.1021/acsnano.3c03103

Author Contributions

H. Ma and S. Kang contributed equally to this work. The manuscript was written through contributions of all authors. All authors have given approval to the final version of the manuscript.

Notes

The authors declare no competing financial interest.

REFERENCES

(1) Bruchez, M., Jr; Moronne, M.; Gin, P.; Weiss, S.; Alivisatos, A. P. Semiconductor Nanocrystals as Fluorescent Biological Labels. *Science* **1998**, *281*, 2013−2016.

(2) Dahmke, I. N.; Verch, A.; Hermannsdörfer, J.; Peckys, D. B.; Weatherup, R. S.; Hofmann, S.; de Jonge, N. Graphene Liquid Enclosure for Single-Molecule Analysis of Membrane Proteins in Whole Cells Using Electron Microscopy. *ACS Nano* **2017**, *11*, 11108−11117.

(3) Carrillo-Carrion, C.; Bocanegra, A. I.; Arnaiz, B.; Feliu, N.; Zhu, D.; Parak, W. J. Triple-Labeling of Polymer-Coated Quantum Dots and Adsorbed Proteins for Tracing their Fate in Cell Cultures. *ACS Nano* **2019**, *13*, 4631−4639.

(4) Kagan, C. R.; Lifshitz, E.; Sargent, E. H.; Talapin, D. V. Building Devices from Colloidal Quantum Dots. *Science* **2016**, *353*, aac5523−aac5523.

(5) Huang, J.; Mulfort, K. L.; Du, P.; Chen, L. X. Photodriven Charge Separation Dynamics in CdSe/ZnS Core/Shell Quantum Dot/Cobaloxime Hybrid for Efficient Hydrogen Production. *J. Am. Chem. Soc.* **2012**, *134*, 16472−16475.

(6) Padgaonkar, S.; Brown, P. T.; Jeong, Y.; Cherqui, C.; Avanaki, K. N.; López-Arteaga, R.; Irgen-Gioro, S.; Wu, Y.; Sangwan, V. K.; Schatz, G. C.; Hersam, M. C.; Weiss, E. A. Mechanism of Long-Range Energy Transfer from Quantum Dots to Black Phosphorus. *J. Phys. Chem. C* **2021**, *125*, 15458−15464.

(7) Huang, J.; Mulfort, K. L.; Du, P.; Chen, L. X. Photodriven Charge Separation Dynamics in CdSe/ZnS Core/Shell Quantum Dot/Cobaloxime Hybrid for Efficient Hydrogen Production. *J. Am. Chem. Soc.* **2012**, *134*, 16472−16475.

(8) Jin, L.; Zhao, H.; Wang, Z. M.; Rosei, F. Quantum Dots-Based Photoelectrochemical Hydrogen Evolution from Water Splitting. *Adv. Energy Mater.* **2021**, *11*, 2003233.

(9) Zhou, X.; Ma, Y.; Ge, Y.; Zhu, S.; Cui, Y.; Chen, B.; Liao, L.; Yun, Q.; He, Z.; Long, H.; Li, L.; Huang, B.; Luo, Q.; Zhai, L.; Wang, X.; Bai, L.; Wang, G.; Guan, Z.; Chen, Y.; Lee, C.-S.; et al. Preparation of Au@Pd Core-Shell Nanorods with Fcc-2H-Fcc Heterophase for Highly Efficient Electrocatalytic Alcohol Oxidation. *J. Am. Chem. Soc.* **2022**, *144*, 547−555.

(10) Murray, C. B.; Norris, D. J.; Bawendi, M. G. Synthesis and Characterization of Nearly Monodisperse CdE (E = Sulfur, Selenium, Tellurium) Semiconductor Nanocrystallites. *J. Am. Chem. Soc.* **1993**, *115*, 8706−8715.

(11) Alivisatos, A. P. Semiconductor Clusters, Nanocrystals, and Quantum Dots. *Science* **1996**, *271*, 933−937.

(12) Lee, J.; Yang, J.; Kwon, S. G.; Hyeon, T. Nonclassical Nucleation and Growth of Inorganic Nanoparticles. *Nat. Rev. Mater.* **2016**, *1*, 16034.

(13) Dai, Q.; Wang, Y.; Zhang, Y.; Li, X.; Li, R.; Zou, B.; Seo, J.; Wang, Y.; Liu, M.; Yu, W. W. Stability Study of PbSe Semiconductor Nanocrystals over Concentration, Size, Atmosphere, and Light Exposure. *Langmuir* **2009**, *25*, 12320−12324.

(14) Ravi, V. K.; Saikia, S.; Yadav, S.; Nawale, V. V.; Nag, A. CsPbBr₃/ZnS Core/Shell Type Nanocrystals for Enhancing Luminescence Lifetime and Water Stability. *ACS Energy Lett.* **2020**, *5*, 1794−1796.

(15) Mocatta, D.; Cohen, G.; Schattner, J.; Millo, O.; Rabani, E.; Banin, U. Heavily Doped Semiconductor Nanocrystal Quantum Dots. *Science* **2011**, *332*, 77−81.

(16) Han, H.; Yao, Y.; Robinson, R. D. Interplay between Chemical Transformations and Atomic Structure in Nanocrystals and Nanoclusters. *Acc. Chem. Res.* **2021**, *54*, 509−519.

(17) Gan, X. Y.; Sen, R.; Millstone, J. E. Connecting Cation Exchange and Metal Deposition Outcomes via Hume−Rothery-Like Design Rules Using Copper Selenide Nanoparticles. *J. Am. Chem. Soc.* **2021**, *143*, 8137−8144.

(18) Thompson, S. M.; Şahin, C.; Yang, S.; Flatté, M. E.; Murray, C. B.; Bassett, L. C.; Kagan, C. R. Red Emission from Copper-Vacancy Color Centers in Zinc Sulfide Colloidal Nanocrystals. *ACS Nano* **2023**, *17*, 5963−5973.

(19) Cordero, S. R.; Carson, P. J.; Estabrook, R. A.; Strouse, G. F.; Buratto, S. K. Photo-Activated Luminescence of CdSe Quantum Dot Monolayers. *J. Phys. Chem. B* **2000**, *104*, 12137−12142.

(20) Hu, Z.; Shu, Y.; Qin, H.; Hu, X.; Peng, X. Water Effects on Colloidal Semiconductor Nanocrystals: Correlation of Photophysics and Photochemistry. *J. Am. Chem. Soc.* **2021**, *143*, 18721−18732.

(21) Ye, X.; Zheng, C.; Chen, J.; Gao, Y.; Murray, C. B. Using Binary Surfactant Mixtures to Simultaneously Improve the Dimensional Tunability and Monodispersity in the Seeded Growth of Gold Nanorods. *Nano Lett.* **2013**, *13*, 765−771.

(22) Kovalenko, M. V.; Manna, L.; Cabot, A.; Hens, Z.; Talapin, D. V.; Kagan, C. R.; Klimov, V. I.; Rogach, A. L.; Reiss, P.; Milliron, D. J.; Guyot-Sionnnest, P.; Konstantatos, G.; Parak, W. J.; Hyeon, T.; Korgel, B. A.; Murray, C. B.; Heiss, W. Prospects of Nanoscience with Nanocrystals. *ACS Nano* **2015**, *9*, 1012−1057.

(23) Whitehead, C. B.; Finke, R. G. Particle Formation Mechanisms Supported by in Situ Synchrotron XAFS and SAXS Studies: A Review of Metal, Metal-Oxide, Semiconductor and Selected Other Nanoparticle Formation Reactions. *Mater. Adv.* **2021**, *2*, 6532−6568.

(24) Korpanty, J.; Parent, L. R.; Hampu, N.; Weigand, S.; Gianneschi, N. C. Thermoresponsive Polymer Assemblies via Variable Temperature Liquid-Phase Transmission Electron Microscopy and Small Angle X-Ray Scattering. *Nat. Commun.* **2021**, *12*, 6568.

(25) Domizio, G. A. D.; Alameda, L. T.; Fanghanel, J.; Lord, R. W.; Miller, J. R.; Schaak, R. E. Real-Time Monitoring of Competing Nanoparticle Formation Pathways during Cation Exchange Using Benchtop Light Scattering. *Chem. Mater.* **2021**, *33*, 3936−3944.

(26) Yang, J.; Siempelkamp, B. D.; Liu, D.; Kelly, T. L. Investigation of CH$_3$NH$_3$PbI$_3$ Degradation Rates and Mechanisms in Controlled Humidity Environments Using in Situ Techniques. *ACS Nano* **2015**, *9*, 1955−1963.

(27) Babbe, F.; Sutter-Fella, C. M. Optical Absorption-based in Situ Characterization of Halide Perovskites. *Adv. Energy Mater.* **2020**, *10*, 1903587.

(28) De Yoreo, J. J.; Gilbert, P. U. P. A.; Sommerdijk, N. A. J. M.; Penn, R. L.; Whitelam, S.; Joester, D.; Zhang, H.; Rimer, J. D.; Navrotsky, A.; Banfield, J. F.; Wallace, A. F.; Michel, F. M.; Meldrum, F. C.; Cölfen, H.; Dove, P. M. Crystallization by Particle Attachment in Synthetic, Biogenic, and Geologic Environments. *Science* **2015**, *349*, aaa6760.

(29) Sohn, S.; Xie, Y.; Jung, Y.; Schroers, J.; Cha, J. J. Tailoring Crystallization Phases in Metallic Glass Nanorods via Nucleus Starvation. *Nat. Commun.* **2017**, *8*, 1980.

(30) Loh, N. D.; Sen, S.; Bosman, M.; Tan, S. F.; Zhong, J.; Nijhuis, C. A.; Král, P.; Matsudaira, P.; Mirsaidov, U. Multistep Nucleation of Nanocrystals in Aqueous Solution. *Nat. Chem.* **2017**, *9*, 77−82.

(31) Zhu, C.; Liang, S.; Song, E.; Zhou, Y.; Wang, W.; Shan, F.; Shi, Y.; Hao, C.; Yin, K.; Zhang, T.; Liu, J.; Zheng, H.; Sun, L. In-Situ Liquid Cell Transmission Electron Microscopy Investigation on Oriented Attachment of Gold Nanoparticles. *Nat. Commun.* **2018**, *9*, 421.

(32) Liu, C.; Ou, Z.; Zhou, S.; Chen, Q. Nonclassical Crystallization Observed by Liquid-Phase Transmission Electron Microscopy. In *ACS Symposium Series*; American Chemical Society: Washington, DC, 2020; pp 115−146.

(33) Jehannin, M.; Rao, A.; Cölfen, H. New Horizons of Nonclassical Crystallization. *J. Am. Chem. Soc.* **2019**, *141*, 10120−10136.

(34) Manna, L.; Cheon, J.; Schaak, R. E. Why Do We Care about Studying Transformations in Inorganic Nanocrystals? *Acc. Chem. Res.* **2021**, *54*, 1543−1544.

(35) Woehl, T. J.; Evans, J. E.; Arslan, I.; Ristenpart, W. D.; Browning, N. D. Direct in Situ Determination of the Mechanisms Controlling Nanoparticle Nucleation and Growth. *ACS Nano* **2012**, *6*, 8599−8610.

(36) Liao, H.-G.; Zherebetskyy, D.; Xin, H.; Czarnik, C.; Ercius, P.; Elmlund, H.; Pan, M.; Wang, L.-W.; Zheng, H. Facet Development during Platinum Nanocube Growth. *Science* **2014**, *345*, 916−919.

(37) Hutzler, A.; Schmutzler, T.; Jank, M. P. M.; Branscheid, R.; Unruh, T.; Spiecker, E.; Frey, L. Unravelling the Mechanisms of Gold-Silver Core-Shell Nanostructure Formation by in Situ TEM Using an Advanced Liquid Cell Design. *Nano Lett.* **2018**, *18*, 7222−7229.

(38) Chen, L.; Leonardi, A.; Chen, J.; Cao, M.; Li, N.; Su, D.; Zhang, Q.; Engel, M.; Ye, X. Imaging the Kinetics of Anisotropic Dissolution of Bimetallic Core-Shell Nanocubes Using Graphene Liquid Cells. *Nat. Commun.* **2020**, *11*, 3041.

(39) Song, M.; Zhou, G.; Lu, N.; Lee, J.; Nakouzi, E.; Wang, H.; Li, D. Oriented Attachment Induces Fivefold Twins by Forming and Decomposing High-Energy Grain Boundaries. *Science* **2020**, *367*, 40−45.

(40) Albrecht, W.; Aert, S. V.; Bals, S. Three-Dimensional Nanoparticle Transformations Captured by an Electron Microscope. *Acc. Chem. Res.* **2021**, *54*, 1189−1199.

(41) Sutter, E. A.; Sutter, P. W. Determination of Redox Reaction Rates and Orders by in Situ Liquid Cell Electron Microscopy of Pd and Au Solution Growth. *J. Am. Chem. Soc.* **2014**, *136*, 16865−16870.

(42) Woehl, T. J.; Abellan, P. Defining the Radiation Chemistry during Liquid Cell Electron Microscopy to Enable Visualization of Nanomaterial Growth and Degradation Dynamics. *J. Microsc.* **2017**, *265*, 135−147.

(43) Jungjohann, K. L.; Bliznakov, S.; Sutter, P. W.; Stach, E. A.; Sutter, E. A. In Situ Liquid Cell Electron Microscopy of the Solution Growth of Au-Pd Core-Shell Nanostructures. *Nano Lett.* **2013**, *13*, 2964−2970.

(44) Yan, C.; Byrne, D.; Ondry, J. C.; Kahnt, A.; Moreno-Hernandez, I. A.; Kamat, G. A.; Liu, Z.-J.; Laube, C.; Crook, M. F.; Zhang, Y.; Ercius, P.; Alivisatos, A. P. Facet-Selective Etching Trajectories of Individual Semiconductor Nanocrystals. *Sci. Adv.* **2022**, *8*, eabq1700.

(45) Ring, E. A.; de Jonge, N. Microfluidic System for Transmission Electron Microscopy. *Microsc. Microanal.* **2010**, *16*, 622−629.

(46) Dunn, G.; Adiga, V. P.; Pham, T.; Bryant, C.; Horton-Bailey, D. J.; Belling, J. N.; LaFrance, B.; Jackson, J. A.; Barzegar, H. R.; Yuk, J. M.; Aloni, S.; Crommie, M. F.; Zettl, A. Graphene-Sealed Flow Cells for in Situ Transmission Electron Microscopy of Liquid Samples. *ACS Nano* **2020**, *14*, 9637−9643.

(47) Ross, F. M. Opportunities and Challenges in Liquid Cell Electron Microscopy. *Science* **2015**, *350*, aaa9886.

(48) Yuk, J. M.; Park, J.; Ercius, P.; Kim, K.; Hellebusch, D. J.; Crommie, M. F.; Lee, J. Y.; Zettl, A.; Alivisatos, A. P. High-Resolution EM of Colloidal Nanocrystal Growth Using Graphene Liquid Cells. *Science* **2012**, *336*, 61−64.

(49) Ghodsi, S. M.; Megaridis, C. M.; Shahbazian-Yassar, R.; Shokuhfar, T. Advances in Graphene-based Liquid Cell Electron Microscopy: Working Principles, Opportunities, and Challenges. *Small Methods* **2019**, *3*, 1900026.

(50) Wang, C.; Qiao, Q.; Shokuhfar, T.; Klie, R. F. High-Resolution Electron Microscopy and Spectroscopy of Ferritin in Biocompatible Graphene Liquid Cells and Graphene Sandwiches. *Adv. Mater.* **2014**, *26*, 3410−3414.

(51) Textor, M.; de Jonge, N. Strategies for Preparing Graphene Liquid Cells for Transmission Electron Microscopy. *Nano Lett.* **2018**, *18*, 3313−3321.

(52) Kelly, D. J.; Clark, N.; Zhou, M.; Gebauer, D.; Gorbachev, R. V.; Haigh, S. J. In Situ TEM Imaging of Solution-Phase Chemical Reactions Using 2D-Heterostructure Mixing Cells. *Adv. Mater.* **2021**, *33*, 2100668.

(53) Clark, N.; Kelly, D. J.; Zhou, M.; Zou, Y.-C.; Myung, C. W.; Hopkinson, D. G.; Schran, C.; Michaelides, A.; Gorbachev, R.; Haigh, S. J. Tracking Single Adatoms in Liquid in a Transmission Electron Microscope. *Nature* **2022**, *609*, 942−947.

(54) Yang, J.; Choi, M. K.; Sheng, Y.; Jung, J.; Bustillo, K.; Chen, T.; Lee, S.-W.; Ercius, P.; Kim, J. H.; Warner, J. H.; Chan, E. M.; Zheng, H. MoS$_2$ Liquid Cell Electron Microscopy through Clean and Fast Polymer-Free MoS$_2$ Transfer. *Nano Lett.* **2019**, *19*, 1788−1795.

(55) Hauwiller, M. R.; Ondry, J. C.; Chan, C. M.; Khandekar, P.; Yu, J.; Alivisatos, A. P. Gold Nanocrystal Etching as a Means of Probing the Dynamic Chemical Environment in Graphene Liquid Cell Electron Microscopy. *J. Am. Chem. Soc.* **2019**, *141*, 4428−4437.

(56) Ye, X.; Jones, M. R.; Frechette, L. B.; Chen, Q.; Powers, A. S.; Ercius, P.; Dunn, G.; Rotskoff, G. M.; Nguyen, S. C.; Adiga, V. P.; Zettl, A.; Rabani, E.; Geissler, P. L.; Alivisatos, A. P. Single-Particle Mapping of Nonequilibrium Nanocrystal Transformations. *Science* **2016**, *354*, 874−877.

(57) Hutzler, A.; Fritsch, B.; Jank, M. P. M.; Branscheid, R.; Martens, R. C.; Spiecker, E.; März, M. In Situ Liquid Cell TEM Studies on Etching and Growth Mechanisms of Gold Nanoparticles at

a Solid−Liquid−Gas Interface. *Adv. Mater. Interfaces* **2019**, *6*, 1901027.

(58) Son, J. S.; Park, K.; Kwon, S. G.; Yang, J.; Choi, M. K.; Kim, J.; Yu, J. H.; Joo, J.; Hyeon, T. Dimension-Controlled Synthesis of CdS Nanocrystals: From 0D Quantum Dots to 2D Nanoplates. *Small* **2012**, *8*, 2394−2402.

(59) Meyer, J. C.; Eder, F.; Kurasch, S.; Skakalova, V.; Kotakoski, J.; Park, H. J.; Roth, S.; Chuvilin, A.; Eyhusen, S.; Benner, G.; Krasheninnikov, A. V.; Kaiser, U. Accurate Measurement of Electron Beam Induced Displacement Cross Sections for Single-Layer Graphene. *Phys. Rev. Lett.* **2012**, *108*, 196102.

(60) Hu, Y.; Cao, Q.; Neumann, C.; Lehnert, T.; Börrnert, F.; Wang, Y.; Kaiser, U.; Turchanin, A.; Eigler, S. Wet-Chemical Synthesis of Solution-Processable Porous Graphene via Defect-Driven Etching. *Carbon N. Y.* **2021**, *185*, 568−577.

(61) Regan, W.; Alem, N.; Alemán, B.; Geng, B.; Girit, Ç.; Maserati, L.; Wang, F.; Crommie, M.; Zettl, A. A Direct Transfer of Layer-Area Graphene. *Appl. Phys. Lett.* **2010**, *96*, 113102.

(62) Keskin, S.; Pawell, C.; de Jonge, N. Verification of Water Presence in Graphene Liquid Cells. *Micron* **2021**, *149*, 103109.

(63) Wang, C.; Shokuhfar, T.; Klie, R. F. Precise in Situ Modulation of Local Liquid Chemistry via Electron Irradiation in Nanoreactors Based on Graphene Liquid Cells. *Adv. Mater.* **2016**, *28*, 7716−7722.

(64) Ghodsi, S. M.; Sharifi-Asl, S.; Rehak, P.; Král, P.; Megaridis, C. M.; Shahbazian-Yassar, R.; Shokuhfar, T. Assessment of Pressure and Density of Confined Water in Graphene Liquid Cells. *Adv. Mater. Interfaces* **2020**, *7*, 1901727.

(65) Senga, R.; Suenaga, K. Single-Atom Electron Energy Loss Spectroscopy of Light Elements. *Nat. Commun.* **2015**, *6*, 7943.

(66) Kang, S.; Kim, J.-H.; Lee, M.; Yu, J. W.; Kim, J.; Kang, D.; Baek, H.; Bae, Y.; Kim, B. H.; Kang, S.; Shim, S.; Park, S.-J.; Lee, W. B.; Hyeon, T.; Sung, J.; Park, J. Real-Space Imaging of Nanoparticle Transport and Interaction Dynamics by Graphene Liquid Cell TEM. *Sci. Adv.* **2021**, *7*, eabi5419.

(67) Sagert, N. H.; MacFarlane, R.; Kremers, W. Gamma Radiolysis of Toluene and Deuterated Toluenes—I. Isotopic Exchange. *Int. J. Radiat. Appl. Instrum. C Radiat. Phys. Chem.* **1991**, *38*, 407−411.

(68) Lazar, P.; Karlický, F.; Jurečka, P.; Kocman, M.; Otyepková, E.; Šafářová, K.; Otyepka, M. Adsorption of Small Organic Molecules on Graphene. *J. Am. Chem. Soc.* **2013**, *135*, 6372−6377.

(69) Jeon, S.; Heo, T.; Hwang, S.-Y.; Ciston, J.; Bustillo, K. C.; Reed, B. W.; Ham, J.; Kang, S.; Kim, S.; Lim, J.; Lim, K.; Kim, J. S.; Kang, M.-H.; Bloom, R. S.; Hong, S.; Kim, K.; Zettl, A.; Kim, W. Y.; Ercius, P.; Park, J.; et al. Reversible Disorder-Order Transitions in Atomic Crystal Nucleation. *Science* **2021**, *371*, 498−503.

(70) Yang, J.; Koo, J.; Kim, S.; Jeon, S.; Choi, B. K.; Kwon, S.; Kim, J.; Kim, B. H.; Lee, W. C.; Lee, W. B.; Lee, H.; Hyeon, T.; Ercius, P.; Park, J. Amorphous-Phase-Mediated Crystallization of Ni Nanocrystals Revealed by High-Resolution Liquid-Phase Electron Microscopy. *J. Am. Chem. Soc.* **2019**, *141*, 763−768.

(71) Zhang, X.; Lea, A. S.; Chaka, A. M.; Loring, J. S.; Mergelsberg, S. T.; Nakouzi, E.; Qafoku, O.; De Yoreo, J. J.; Schaef, H. T.; Rosso, K. M. In Situ Imaging of Amorphous Intermediates during Brucite Carbonation in Supercritical CO_2. *Nat. Mater.* **2022**, *21*, 345−351.

(72) Smeets, P. J. M.; Cho, K. R.; Kempen, R. G. E.; Sommerdijk, N. A. J. M.; De Yoreo, J. J. Calcium Carbonate Nucleation Driven by Ion Binding in a Biomimetic Matrix Revealed by in Situ Electron Microscopy. *Nat. Mater.* **2015**, *14*, 394−399.

(73) Wanrooij, P. H. P.; Agarwal, U. S.; Meuldijk, J.; van Kasteren, J. M. N.; Lemstra, P. J. Extraction of CdS Pigment from Waste Polyethylene. *J. Appl. Polym. Sci.* **2006**, *100*, 1024−1031.

(74) Aslam, R.; Müller, K.; Arlt, W. Experimental Study of Solubility of Water in Liquid Organic Hydrogen Carriers. *J. Chem. Eng. Data* **2015**, *60*, 1997−2002.

(75) Manna, L.; Wang, L. W.; Cingolani, R.; Alivisatos, A. P. First-Principles Modeling of Unpassivated and Surfactant-Passivated Bulk Facets of Wurtzite CdSe: A Model System for Studying the Anisotropic Growth of CdSe Nanocrystals. *J. Phys. Chem. B* **2005**, *109*, 6183−6192.

(76) Schneider, N. M.; Norton, M. M.; Mendel, B. J.; Grogan, J. M.; Ross, F. M.; Bau, H. H. Electron−Water Interactions and Implications for Liquid Cell Electron Microscopy. *J. Phys. Chem. C* **2014**, *118*, 22373−22382.

(77) Sutter, E.; Jungjohann, K.; Bliznakov, S.; Courty, A.; Maisonhaute, E.; Tenney, S.; Sutter, P. In Situ Liquid-Cell Electron Microscopy of Silver-Palladium Galvanic Replacement Reactions on Silver Nanoparticles. *Nat. Commun.* **2014**, *5*, 4946.

(78) Tully, F. P.; Ravishankara, A. R.; Thompson, R. L.; Nicovich, J. M.; Shah, R. C.; Kreutter, N. M.; Wine, P. H. Kinetics of the Reactions of Hydroxyl Radical with Benzene and Toluene. *J. Phys. Chem.* **1981**, *85*, 2262−2269.